

Thermoelectric properties of ultrathin silicon nanowires

E. B. Ramayya,* L. N. Maurer, A. H. Davoody, and I. Knezevic†

Department of Electrical and Computer Engineering, University of Wisconsin-Madison, Madison, Wisconsin 53706, USA

(Received 20 October 2011; revised manuscript received 23 July 2012; published 24 September 2012)

We calculate the room-temperature thermoelectric properties of highly doped ultrathin silicon nanowires (SiNW) of square cross section (3×3 to 8×8 nm²) by solving the Boltzmann transport equations for electrons and phonons on an equal footing, using the ensemble Monte Carlo technique for each. We account for the two-dimensional confinement of both electrons and phonons and all the relevant scattering mechanisms, and present data for the dependence of electrical conductivity, the electronic and phononic thermal conductivities, the electronic and phonon-drag Seebeck coefficients, as well as the thermoelectric figure of merit (ZT) on the SiNW rms roughness and thickness. ZT in ultrascaled SiNWs does not increase as drastically with decreasing wire cross section as suggested by earlier studies. The reason is surface roughness, which (beneficially) degrades thermal conductivity, but also (adversely) degrades electrical conductivity and offsets the Seebeck coefficient enhancement that comes from confinement. Overall, room-temperature ZT of ultrathin SiNWs varies slowly with thickness, having a soft maximum of about 0.4 at the nanowire thickness of 4 nm.

DOI: [10.1103/PhysRevB.86.115328](https://doi.org/10.1103/PhysRevB.86.115328)

PACS number(s): 72.20.Pa, 84.60.Rb, 73.63.Nm, 65.80.-g

I. INTRODUCTION

Thermoelectric (TE) phenomena include conversion of electricity to heat and heat to electricity using solid-state devices.¹⁻³ Suitability of a material for thermoelectric applications at temperature T is judged from its figure of merit $ZT = S^2\sigma T/\kappa$, where S , σ , and κ are the Seebeck coefficient (thermopower), electrical conductivity, and thermal conductivity, respectively. Highly doped semiconductors make the best thermoelectric materials^{4,5} because heat is carried predominantly by the lattice, so thermal conductivity κ is largely decoupled from the power factor $S^2\sigma$. $ZT > 3.0$ is required to replace conventional chlorofluorocarbon (CFC) coolers by TE coolers, but increasing ZT of bulk semiconductors beyond 1.0 has been a challenge.⁴

Ideally, we want to improve the power factor $S^2\sigma$ while simultaneously reducing thermal conductivity κ .⁶ Nanostructuring could, in principle, bring about both of these benefits.^{7,8} On the one hand, inclusion of various size nanostructured obstacles can scatter phonons of different wavelengths and quench conduction of heat. Indeed, high figures of merit due to low thermal conductivity have been demonstrated on materials incorporating nanoscale inclusions.⁹⁻¹¹ On the other hand, Hicks and Dresselhaus^{12,13} pioneered the concept that nanostructuring, through the modification of the density of states for electrons and holes, could significantly enhance the Seebeck coefficient and consequently the power factor. Nanowires are particularly interesting in this regard because of their sharp density of states. Recent experimental work on rough silicon nanowires^{14,15} demonstrated room temperature $ZT \sim 0.6$, nearly two orders of magnitude above the bulk-silicon value of $ZT = 0.01$. These are exciting results as they brought silicon, a cheap and abundant semiconductor, into the realm of plausibility for thermoelectric applications. It is now fairly certain that the enhanced ZT in these experiments came primarily from a drastic thermal conductivity degradation because the wires were very rough (rms roughness even in the nanometer range)¹⁶ and most of them were too thick (20–50 nm) for the quantum confinement effects to be really significant. However, Boukai *et al.*¹⁴ also proposed that the

phonon-drag component in very thin nanowires, especially at lower temperatures, may be responsible in part for the ZT enhancement.

In ultrathin wires, thermal conductivity is expected to be very low, based on theoretical work using molecular dynamics,¹⁷⁻²⁰ nonequilibrium Green's functions in the harmonic approximation,²¹⁻²³ and the Boltzmann transport equation addressing phonon transport.²⁴⁻²⁸ Theoretical work focusing on the electronic part of the picture²⁹⁻³⁴ indicates that confinement benefits to the power factor should be realizable in ultrathin wires; however, they have not been reported experimentally.⁸ Therefore, whether strong confinement in nanowires can indeed bring about both low thermal conductivity and enhanced thermoelectric power factor and whether unusual features such as enhanced phonon drag emerge due to nanostructuring are presently open questions.

In this paper, we present a simulation of electronic and thermal transport in ultrathin square silicon nanowires (cross sections ranging from 3×3 to 8×8 nm²), highly doped and surrounded by a native oxide. Transport of charge and heat is described by solving the Boltzmann transport equations (BTEs) for both electrons and acoustic phonons on an equal footing by using the ensemble Monte Carlo^{35,36} (EMC) technique for each. Electronic states are calculated based on a self-consistent Schrödinger-Poisson solver within the effective mass framework,^{37,38} appropriate for ultrathin wires.^{39,40} Acoustic phonon intravalley, intervalley, ionized impurity, and surface-roughness scattering (according to generalized Ando's model^{38,41-43}) have been accounted for in the electronic transport simulation. In the phonon simulation, we work with bulk instead of confined phonons, as the one-dimensional to three-dimensional (1D to 3D) crossover for wires of thicknesses such as ours happens at temperatures considerably lower than 300 K.⁴⁴ The phonons undergo three-phonon normal and umklapp scattering, impurity, and surface-roughness scattering. In the phonon simulation, the random rough surface of a SiNW is numerically generated based on an autocorrelation length and rms height, and is directly included in the phonon EMC kernel. The wires in this

study are very thin, so we consider rms roughnesses in the range $\Delta = 0.2$ nm [Si/SiO₂ interface quality in the complementary metal-oxide-semiconductor (CMOS) technology] to 0.5 nm. Roughnesses much higher than 0.5 nm would likely mean destruction of ultrathin wires.

Our study shows pronounced decreases in electrical and thermal conductivities with decreasing wire thickness and increasing roughness. As in the bulk, the electronic contribution to thermal conductivity remains negligible with respect to the lattice contribution, and the phonon-drag Seebeck coefficient is much smaller than the electronic one. The electronic Seebeck coefficient increases with decreasing wire thickness; however, the power factor decreases overall, as the decrease in electrical conductivity as the wires become thinner negates the increase in the squared Seebeck coefficient. Overall, the ZT in ultrathin nanowires is greater by a factor 20–40 than the bulk value and its variation with thickness is fairly weak. There is a broad maximum of about 0.4 for the SiNW of thickness 4 nm and a reasonably high rms roughness of 0.5 nm.

This paper is organized as follows: In Sec. II, we present the calculation of electrical conductivity from electronic EMC. In Sec. III, we calculate thermal conductivity and give details on the generation of a random rough surface with a given rms roughness and correlation length for the inclusion in the phonon EMC. The Seebeck coefficient calculation is presented in Sec. IV. In Sec. V, the thermoelectric coefficients calculated in the previous sections are used to compute the ZT in ultrathin SiNWs. In Secs. IV and V, we discuss the influence of surface roughness on the density of states, the Seebeck coefficient, and ZT . We conclude with a brief summary and some final remarks in Sec. VI.

II. ELECTRICAL CONDUCTIVITY

The SiNWs for thermoelectric applications are very highly doped to increase electrical conductivity. The cross sections of the SiNW considered in this study are between 3×3 nm² to 8×8 nm² and the wire is surrounded on all sides by a thermal oxide of thickness 1 nm. The silicon channel is assumed to be n -type doped to 1.6×10^{19} cm⁻³ with arsenic (same as the doping in Ref. 14). Thermoelectric coefficients (the Seebeck coefficient, electrical conductivity, and thermal conductivity, required to estimate the ZT of a material) are calculated by solving the electron and phonon BTEs.

The simulator developed to calculate electrical conductivity has two components: calculation of electronic states across the wire and a transport kernel that finds the distributions in those states. Electronic states are found from a self-consistent 2D Poisson–2D Schrödinger solver within the effective mass framework,^{37,38} shown to be valid for the wire cross sections in this study.⁴⁰ The electronic band structure in SiNWs is altered from that of bulk silicon due to 2D confinement.^{45–48} This effect is included through the effective mass and the band-gap variation extracted from the band structure obtained using $sp^3d^5s^*$ tight-binding model.^{39,46,48} The finite barrier at the Si/SiO₂ interface results in the electron wave-function penetration through the interface and into the oxide. The electric field and the wave functions are forced to zero at the air/SiO₂ interfaces. The ARPACK package⁴⁹ is used to solve the 2D Schrödinger equation and the successive

over-relaxation (SOR) method is used to solve the 2D Poisson equation.

The EMC transport kernel^{37,38,50,51} is used to simulate electron transport along the wire axis under the influence of a low lateral electric field. The long wire approximation implies that the transport is diffusive (the length exceeds the carrier mean-free path) and therefore justifies the use of the ensemble Monte Carlo method^{35,36} to simulate electron transport. Electrons are initialized such that their average kinetic energy is $(1/2)k_B T$ (thermal energy for 1D) and are distributed among different subbands in accordance with the equilibrium distribution of the states obtained from the Poisson–Schrödinger solver. Since the electrons are confined in two transverse directions, they are only scattered in either the forward or the backward direction; consequently, just the carrier momentum along the wire needs to be updated after each scattering event. The doping level is in the degenerate limit, therefore the Pauli exclusion principle is included in the Monte Carlo simulation via the rejection technique.⁵² It is incorporated by checking if the final state is empty before scattering. The electron is allowed to undergo a scattering event only if the final state is empty; if not, the scattering event is treated as self-scattering.⁵² Upon reaching a steady state (indicated by the saturation of the average electron energy and drift velocity), conductivity is calculated from the ensemble average of the electron velocities.³⁵

The roughness at the Si/SiO₂ interface is well described by an exponentially varying autocorrelation function, defined by a rms roughness Δ and a correlation length Λ .⁵³ The rate of surface-roughness scattering (SRS) is calculated from Ando’s model,⁴¹ modified to account for the 2D confinement of electrons in SiNWs.^{42,43} The derivations and expressions used for the SRS and phonon scattering rates can be found in Ref. 38. We assume the correlation length to be 2.5 nm as in CMOS interfaces,⁵³ but it is likely even lower in chemically roughened SiNWs. As the wires we consider throughout this paper are very thin (3×3 to 8×8 nm²), the roughness rms height can not be excessive. The rms roughness of CMOS-quality Si/SiO₂ interfaces is about 0.2 nm, which we take as the lower realistic limit. We assume the upper limit in intentionally roughened ultrathin wires to be 0.5 nm, which is considerable given their size (in contrast, the wires in Ref. 15 are much thicker, ~ 50 nm, and their rms roughness appears to be as high as several nanometers¹⁶).

As the wires considered for thermoelectric applications are heavily doped, scattering from ionized impurities is expected to play a crucial role in determining electrical conductivity σ . Therefore, in addition to SRS and phonon scattering,^{37,38,54} scattering due to impurities is also included in the calculation of σ . At densities above 10^{19} cm⁻³, the Debye–Hückel model for screening has been shown to overestimate the mobility, therefore we use degenerate Thomas–Fermi screening in the calculation of impurity scattering.^{55,56} The use of a degenerate screening length has been shown to give the correct mobility behavior at high doping densities.^{55,56} The expression for the electron-impurity scattering rate is derived in the Appendix.

It is also worth noting that scattering of electrons from confined phonons in lightly doped wires reduces the mobility by about 10% with respect to scattering from unconfined

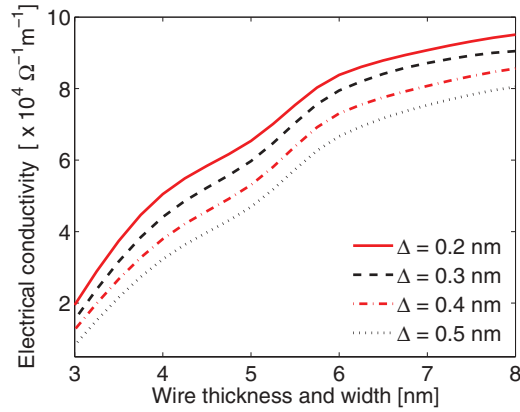


FIG. 1. (Color online) Electrical conductivity in square SiNWs as a function of the wire cross section for different interface roughness rms heights Δ ($\Lambda = 2.5$ nm). The rapid drop in conductivity for the wires of cross section below 6×6 nm² occurs because of a significant increase in surface-roughness scattering.

phonons, but phonon confinement plays a negligible role in the calculation of electrical conductivity in thin, highly doped wires.³⁸

The calculated electrical conductivity as a function of the wire cross section and rms roughness at the Si/SiO₂ interface is shown in Fig. 1. Electrical conductivity in SiNWs decreases with decreasing wire cross section and increasing rms roughness at the interface. For relatively large wires, intervalley phonon and impurity scattering dominate electronic transport. For ultrathin wires (below the 6×6 nm² cross-sectional area), the rolloff in σ occurs because of the rapid increase in the confinement-induced part of SRS.³⁸ Except for the impurity scattering rate calculation, which is presented in Appendix A, all the other details of the electrical conductivity calculation have been documented in detail in Refs. 38 and 57.

III. THERMAL CONDUCTIVITY

Electrons and phonons both contribute to thermal conductivity. The lattice thermal conductivity (κ_l) is calculated by solving the phonon BTE using the ensemble Monte Carlo technique. The electronic contribution to thermal conductivity is calculated by solving the 1D electron BTE under the relaxation-time approximation (RTA).

A. Ensemble Monte Carlo for phonon transport in SiNWs

The EMC phonon transport kernel can treat the normal (N) and umklapp (U) three-phonon scattering processes separately. This fact is important because only the U processes (net momentum in the case of U processes is conserved up to an integer multiple of a reciprocal lattice vector) directly affect the heat conduction, whereas the N processes (net momentum is conserved) aid the U processes indirectly by redistributing phonons among different branches, thereby increasing or decreasing the probability of a U process.

The use of EMC also enables us to treat surface-roughness scattering of phonons in real space: an actual surface, defined by an exponential autocorrelation length and rms roughness,

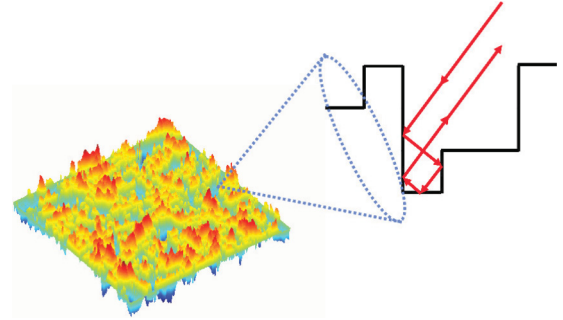


FIG. 2. (Color online) An exponentially correlated surface generated using FFT for $\Delta = 0.25$ nm and $\Lambda = 5$ nm. (Inset) A sample trajectory of a phonon hitting a groove in the surface and spending some time bouncing around before getting out.

can be directly included in the EMC kernel. Since phonon-boundary scattering is the dominant mechanism by which phonons are randomized in ultrathin wires, the use of a real-space random surface rather than a specular parameter becomes very important. When a phonon hits a rough surface, it spends some time bouncing around before entering the wire again. Employment of a real surface in a way captures the localization of phonons.⁵⁸ A sample trajectory of a phonon getting temporarily localized near a rough boundary is shown in the right panel of Fig. 2.

At room temperature, the average wavelength of acoustic phonons is about 1 nm; therefore, spatial confinement has little effect on them for the cross sections considered in this study and we treat them as bulk phonons. The bulk-phonon approximation has also been shown to be valid for the purposes of phonon transport in a recent detailed study by Prasher *et al.*⁴⁴ In their work, they showed that the bulk-to-1D transition for phonons in SiNWs of diameters 2.7 and 10.8 nm happens roughly below 24.1 and 6.4 K, respectively.

The EMC procedure used in this work is similar to the one described by Refs. 25 and 59–61, but we have used a real-space rough boundary in our study.

1. Phonon scattering rates

In addition to surface-roughness scattering of phonons, which we discuss in detail below, we account for phonon-phonon scattering and impurity scattering (including mass difference and dopant scattering). The total impurity scattering rate of a phonon of angular frequency ω is given by

$$\Gamma_I(\omega) = (A_{\text{iso}} + A_{\delta R} + A_{\delta M})\omega^4, \quad (1)$$

where $A_{\text{iso}} = 1.32 \times 10^{-45}$ s³ is the isotope scattering constant (from Ref. 62), while $A_{\delta R} = 5.44 \times 10^{-46}$ s³ and $A_{\delta M} = 5.42 \times 10^{-45}$ s³ are the constants associated with the mass difference and change in relative displacements due to dopants, and the values have been taken from Ref. 63 for the doping density of 1.6×10^{19} cm⁻³.

Phonon-phonon scattering rates are calculated separately for transverse and longitudinal acoustic phonons (subscripts N , U , T , and L denote normal, umklapp, transverse, and longitudinal, respectively) based on the expressions given in

Holland's work:⁶²

$$\Gamma_{TN} = \begin{cases} B_{TN}\omega T^4, & \omega < \omega_{T\text{Amax}} \\ 0, & \omega > \omega_{T\text{Amax}} \end{cases} \quad (2a)$$

$$\Gamma_{TU} = \begin{cases} 0, & \omega < \omega_{1/2} \\ B_{TU} \frac{\omega^2}{\sinh\left(\frac{\hbar\omega}{k_B T}\right)}, & \omega > \omega_{1/2} \end{cases} \quad (2b)$$

$$\Gamma_{LN/U} = B_{LN/U}\omega^2 T^3. \quad (2c)$$

Here, $B_{TN} = 7.44 \times 10^{-13} \text{ K}^{-3}$, $B_{TU} = 4.4 \times 10^{-18} \text{ s}$, and $B_{LN} = B_{LU} = 8 \times 10^{-25} \text{ s K}^{-3}$. The constants were modified to match the thermal conductivity of bulk silicon at room temperature. $\omega_{T\text{Amax}}$ is the frequency at $k = k_{\text{max}}$ (Brillouin zone edge), while $\omega_{1/2}$ is the frequency at $k = k_{\text{max}}/2$.

2. Surface generation

Goodnick *et al.*⁵³ studied the Si/SiO₂ interface with high-resolution transmission electron microscopy (HRTEM) and found it to be well described by an exponential autocorrelation function (ACF). Fast Fourier transform (FFT) is a fast and convenient method for generating surfaces from a given ACF. In this work, we have adopted the method developed by Wu⁶⁴ to generate a rough surface defined by rms Δ and correlation length Λ .

To generate an $M \times N$ surface $Z_{p,q}$, start with a real ACF ($R_{r,s}$). We define $\tilde{R}_{r,s}$ by setting $\tilde{R}_{M-1-r,N-1-s} = \tilde{R}_{M-1-r,s} = \tilde{R}_{r,N-1-s} = \tilde{R}_{r,s} = R_{r,s}$ for all $r = 0, 1, \dots, M/2 - 1$ and $s = 0, 1, \dots, N/2 - 1$. The spectral density $\tilde{S}_{k,i}$ is found using a Fourier transform (\mathcal{F})

$$\tilde{S} = \mathcal{F}(\tilde{R}). \quad (3)$$

Next, we generate $\phi_{k,i}$, a set of random phase angles uniformly distributed in $[0, 2\pi)$. To make $Z_{p,q}$ real, we require:

$$\begin{aligned} \phi_{0,0} &= \phi_{M/2,0} = \phi_{0,N/2} = \phi_{M/2,N/2} = 0, \\ \phi_{M-i,0} &= -\phi_{i,0} \quad i = 1, 2, \dots, M/2 - 1, \\ \phi_{0,N-j} &= -\phi_{0,j} \quad j = 1, 2, \dots, N/2 - 1, \\ \phi_{M-i,N-j} &= -\phi_{i,j} \quad i = 1, 2, \dots, M/2 - 1, j = 1, 2, \dots, N - 1. \end{aligned} \quad (4)$$

Finally, we find Z with an inverse Fourier transform (\mathcal{F}^{-1})

$$Z = \mathcal{F}^{-1}(\sqrt{\tilde{S}}e^{i\phi}). \quad (5)$$

3. Initialization

A wire of a given length is split into a number of cells (here, 20 cells is typical) and phonons in each cell are initialized according to the equilibrium Bose-Einstein distribution for the appropriate temperature. For the thermal conductivity calculation, the first and the last cell are treated as black bodies with a high temperature T_H and low temperature T_L , respectively. All the intermediate cells are initially set to the low temperature as well.

The length of the wire is chosen such that it is much longer than the mean-free path of phonons, so transport can be considered diffusive. For the ultrathin wires considered in this study, the mean-free path is on the order of the wire

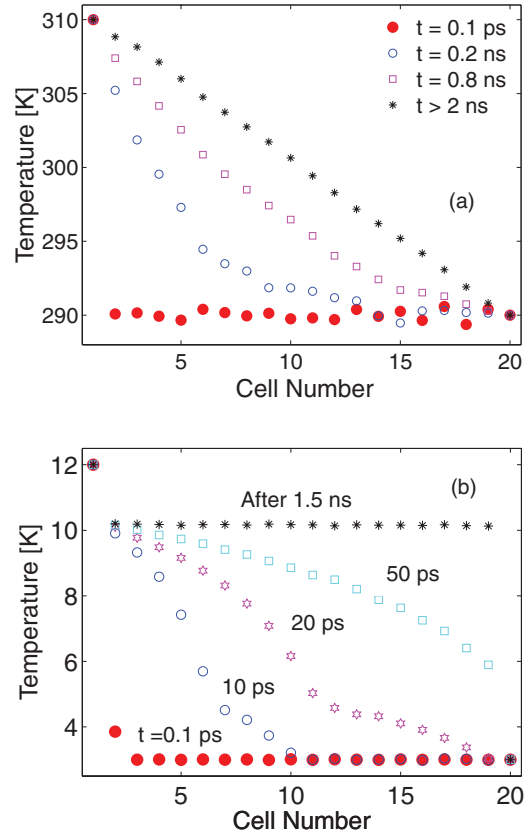


FIG. 3. (Color online) Transient temperature profile along the wire for diffusive and ballistic phonon transport. (a) In the diffusive transport regime, a linear temperature profile is established along the wire when the system reaches a steady state. (b) In the ballistic regime, the steady-state temperature is constant along the wire, with discontinuities at the two end cells.

cross-sectional size (a few nanometers), so the wire length is set to 200 nm. The signature of the diffusive transport limit is a linear temperature drop in the steady state [Fig. 3(a)]. In the opposite, ballistic limit, there is a discontinuity in the temperature profile at the contacts, while the steady-state temperature in the wire T_{ss} is constant throughout and given by the Stefan-Boltzmann law of blackbody radiation: $T_{ss}^B = [(T_H^4 + T_L^4)/2]^{1/4}$ [Fig. 3(b)].^{57,60} The ballistic limit is achieved by turning off all the scattering mechanisms inside the wire (such as by lowering the temperature) and assuming the boundary to be perfectly smooth, so phonons scatter specularly.

The initialization of phonons involves three parts: (1) calculating the number of phonons in the simulation domain; (2) initializing phonon frequencies, wave vectors, and positions; (3) setting up the real-space boundary conditions. Only acoustic phonons are included in the simulation because they are the dominant heat carriers at room temperature. The dispersion of the transverse acoustic (TA) (twofold degenerate, $g_p = 2$) and longitudinal acoustic (LA) ($g_p = 1$) phonons in silicon in the [100] direction has been approximated with a quadratic fit.⁶⁵ From the dispersion and the Bose-Einstein distribution function, the number of phonons N in volume

V at temperature T can be calculated as

$$N = V \sum_{p=LA,TA} \sum_{i=1}^{N_w} \frac{1}{\exp\left(\frac{\hbar\omega_i}{k_B T}\right) - 1} \frac{q_{i,p}^2}{2\pi^2 v_{i,p}} g_p \Delta\omega. \quad (6)$$

Here, V is the volume, N_w is the number of spectral intervals between 0 and ω_{LA}^{\max} with uniform spectral intervals $\Delta\omega = \omega_{LA}^{\max}/N_w$. As the number of phonons N at room temperature is about 10^5 even in a small volume of $(10 \text{ nm})^3$, a weighting factor $W_i \approx 10\text{--}1000$ is used⁵⁹ in the EMC calculation in order to calculate κ_l in a reasonable time, where W_i is the number of phonons corresponding to one simulated phonon. The number of simulated phonons is given by $\tilde{N} = N/W_i$. Once the number of phonons that need to be simulated is calculated, the attributes of each phonon are set.

The frequency ω of each phonon is found from the normalized cumulative number density function which is constructed from the number of phonons N_i in the i th spectral interval and the total number of phonons. Polarization is obtained from the fraction of LA phonons to the total number of phonons in the required spectral interval. From ω and the polarization of the phonon, the magnitude of the wave vector (q) and the group velocity can be calculated using the dispersion relation.⁶⁵ The directional components of \mathbf{q} are set such that phonons are isotropically distributed in the reciprocal space. The position of the phonons is selected to ensure uniform distribution of phonons in each cell of the wire.

4. Phonon free flight and scattering

To calculate the lattice thermal conductivity at 300 K, T_H and T_L are set to 310 and 290 K, respectively (these values of T_L and T_H give a ballistic temperature of about 300 K). After initializing the phonons in each cell with the equilibrium distribution, they are allowed to fly and scatter. The phonon and impurity scattering are treated in the same way as in the previous Monte Carlo (MC) study.²⁵ At the end of a time step Δt , the total energy (E_T) of phonons in each cell is calculated. The new temperature of each cell after Δt is calculated from E_T using numerical inversion of the energy relation to temperature

$$\frac{E_T}{V} W_i = \sum_{p=LA,TA} \sum_{i=1}^{N_w} \frac{\hbar\omega_i}{\exp\left(\frac{\hbar\omega_i}{k_B T}\right) - 1} \frac{q_{i,p}^2}{2\pi^2 v_{i,p}} g_p \Delta\omega. \quad (7)$$

The end cells are reinitialized to their equilibrium distribution after each Δt . Whenever phonons from an intermediate cell hit the end cells, they are absorbed (the phonon is deleted from the simulation). When a phonon hits the rough boundary, it is reflected specularly. The use of a rough boundary automatically takes care of momentum randomization instead of the commonly used specular parameter.⁶⁶ Since the second cell is at a lower temperature than the first cell (which is held at T_H), the heat flux entering it will be higher than the outgoing flux. This discrepancy will result in an increase in the cell's temperature. As the time progresses, the temperature in cells down the line will also increase. In a steady state, a linear temperature profile will be established along the wire axis. Upon reaching a steady state in the wire of length L , Fourier's law is used to calculate κ_l from the net heat flux (Φ ,

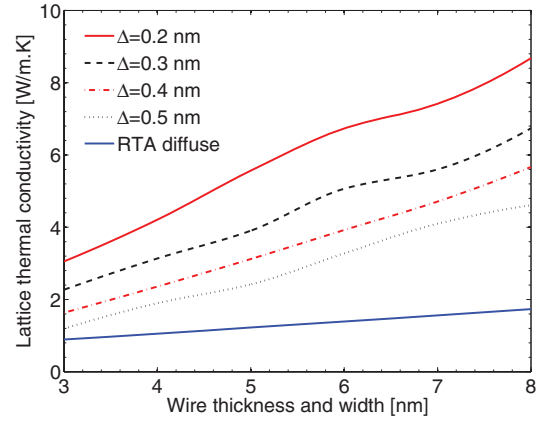


FIG. 4. (Color online) Lattice thermal conductivity as a function of the SiNW cross section for different rms roughness Δ at the Si/SiO₂ interface. Thermal conductivity in SiNWs is more than an order of magnitude smaller than that in bulk silicon because of strong phonon-boundary scattering.

constant along the wire in a steady state) crossing the interface between any two adjoining cells

$$\kappa_l = \frac{\Phi L}{T_H - T_L}. \quad (8)$$

To increase the calculation accuracy, κ_l is calculated from Φ averaged over all the interfaces between cells and over a few thousand time steps once the steady state is reached. At a single interface,

$$\Phi = \frac{W_t}{W^2 \Delta t} \sum_{i=1}^{N_c} \hbar\omega, \quad (9)$$

where W is the width/thickness of the wire (so W^2 is the cross-sectional area) and N_c is the number of phonons crossing the interface between two adjoining cells.

In order to test the free-flight part, we first simulated ballistic phonon transport. For this case, the surface of the wire is smooth (generated by setting $\Delta = 0$) and phonons are allowed to fly with the velocity they gained in the injecting contact. Under ballistic conditions, the steady-state temperature in the wire should be same in all the cells, with a discontinuity at the two end cells.⁶⁷ The ballistic case is tested with $T_H = 12 \text{ K}$ and $T_L = 3 \text{ K}$, which corresponds to $T_{ss}^B = 10.1 \text{ K}$ [see Fig. 3(b)] and shows the transient temperature profile along the wire for the ballistic case. We see that it takes about 1.5 ns to attain the steady-state temperature profile and the $T_{ss}^B \approx 10.1 \text{ K}$ as expected.

B. Lattice thermal conductivity

The lattice thermal conductivity κ_l , calculated using phonon Monte Carlo simulation for varying SiNW cross section and different surface rms roughness, is plotted in Fig. 4. κ_l in SiNW decreases with decreasing wire cross section due to strong phonon-boundary scattering. As expected, increasing rms roughness results in a decrease in κ_l .

We also compare the data to the relaxation-time approximation (RTA) result for thermal conductivity, calculated based

on

$$\kappa_l = \frac{K_B}{\pi W^2} \sum_j \int d\omega \frac{v_j(\omega) \tau_j(\omega) y_j^2(\omega)}{[e^{y_j(\omega)} - 1]^2}, \quad y_j(\omega) = \frac{\hbar \omega_j}{K_B T}. \quad (10)$$

Here, v_j is the phonon velocity and τ_j^{-1} is the sum of the scattering rates due to all scattering mechanisms [phonon-phonon (2), mass-difference (1), and boundary scattering] for a given branch j . Following Lü *et al.*,⁶⁸ the boundary scattering relaxation rate is given by

$$\Gamma_{j,B}(\omega) = \frac{1-p}{1+p} \frac{v_j(\omega) \sqrt{\pi}}{2W}, \quad (11)$$

where p is the specularity parameter whose value, a number between 0 and 1, measures the probability of the phonon being specularly reflected. $p = 0$ corresponds to the diffuse limit, i.e., the outgoing phonon's momentum is completely randomized.⁶⁶ Formally, an extremely large rms roughness (about 3 nm) (Ref. 16) would be required to get the κ_l corresponding to the diffuse limit; such a large rms roughness would clearly be unrealistic in the ultrathin wires considered here without destroying them, but it is a useful limit for comparison. In the case of larger wires, such as those with diameter in the ~ 50 -nm range, considered by Hochbaum *et al.*,¹⁵ the effect of surface roughness on σ is not so pronounced, so κ_l can indeed be preferentially reduced further by roughening the surface.

C. Electronic thermal conductivity

The electronic contribution to thermal conductivity (κ_e) is calculated by solving the electron Boltzmann equation. The expression for κ_e is derived from the 1D electron BTE under the RTA for a wire of cross section $W \times H$ at temperature T is given by

$$\kappa_e = \frac{2\sqrt{\frac{2}{m}}}{\pi \hbar W^2 T} \left[\frac{\sum_{\nu,n} \left\{ \int \sqrt{E} \frac{\partial f_0(E)}{\partial E} (E + E_n^\nu) \tau_n^\nu(E) dE \right\}^2}{\sum_{\nu,n} \int \sqrt{E} \frac{\partial f_0(E)}{\partial E} \tau_n^\nu(E) dE} - \frac{\sum_{\nu,n} \int \sqrt{E} \frac{\partial f_0(E)}{\partial E} (E + E_n^\nu)^2 \tau_n^\nu(E) dE}{\sum_{\nu,n} \int \sqrt{E} \frac{\partial f_0(E)}{\partial E} \tau_n^\nu(E) dE} \right], \quad (12)$$

where $f_0(E)$ is the equilibrium Fermi function at energy E , E_F is the Fermi level, $\tau_n^\nu(E)$ is the relaxation time of electron of charge e , mass m , and energy E in subband n of valley ν , and E_n^ν is the energy of the bottom of that subband. $\tau_n^\nu(E)$ includes all the possible intrasubband, intersubband, and intervalley scattering times.^{38,57}

As in bulk semiconductors, the electronic portion of thermal conductivity is proportional to electrical conductivity and therefore κ_e decreases with a decrease in the wire cross section and an increase in roughness (Fig. 5). κ_e has a negligible effect on the total thermal conductivity in SiNWs, as it is more than an order of magnitude smaller than the lattice thermal conductivity.

IV. SEEBECK COEFFICIENT

The Seebeck coefficient has two components: electronic (S_e) and phononic (S_{ph} , also known as the phonon-drag

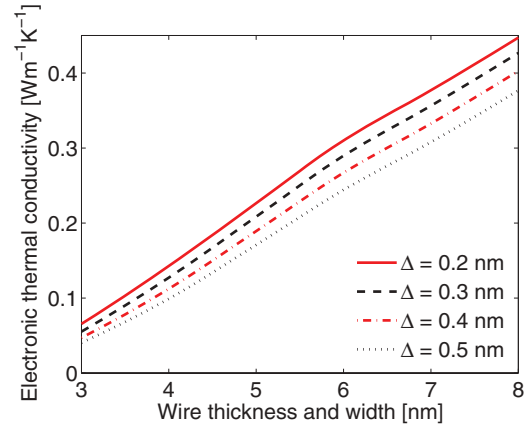


FIG. 5. (Color online) Electronic contribution to thermal conductivity κ_e as a function of the SiNW cross section for different rms roughness Δ at the Si/SiO₂ interface. κ_e follows the same trend as the σ variation with cross section and roughness. As in bulk silicon, κ_e is much smaller than κ_l .

component). S_e is expected to be much larger in nanowires than in bulk materials due to the sharp density of states (DOS) in quasi-1D materials.¹² Also, Boukai *et al.*¹⁴ argued that there is an appreciable phonon-drag contribution to the thermopower in their wires, contributing to the ZT enhancement they observed. In this section, we calculate both components of the Seebeck coefficient in ultrathin SiNWs.

A. Electronic Seebeck coefficient

The expressions for S_e derived from the 1D electron BTE under the RTA are given by

$$S_e = \frac{E_F}{eT} - \frac{1}{eT} \frac{\sum_{\nu,n} \int \sqrt{E} \frac{\partial f_0(E)}{\partial E} (E + E_n^\nu) \tau_n^\nu(E) dE}{\sum_{\nu,n} \int \sqrt{E} \frac{\partial f_0(E)}{\partial E} \tau_n^\nu(E) dE}. \quad (13)$$

The electronic component of the thermopower quantifies the electric field that opposes the diffusion of electrons from the hot side to the cold side. This electric field opposes the applied field in the case of a TE cooler so it reduces the electrical conductivity, therefore S_e drops as σ increases [Fig. 6(a)]. With increasing confinement, the energy separation between the conduction band edge and the Fermi level increases, which results in an increase in the average energy carried by electrons; therefore, the Seebeck coefficient increases as the wire cross section decreases. As in bulk Si, the dominant contribution to the Seebeck coefficient comes from S_e .

B. Phonon-drag Seebeck coefficient

The phononic (i.e., phonon-drag) contribution to the Seebeck coefficient S_{ph} is calculated from the fraction of the electron-acoustic phonon scattering rate to the total electron scattering rate (γ), average velocity of acoustic phonons (v_{ph}), relaxation time of acoustic phonons (τ_{ph}), and the mobility of electrons (μ). S_{ph} is given by

$$S_{ph} = \frac{\gamma v_{ph}^2 \tau_{ph}}{\mu T}. \quad (14)$$

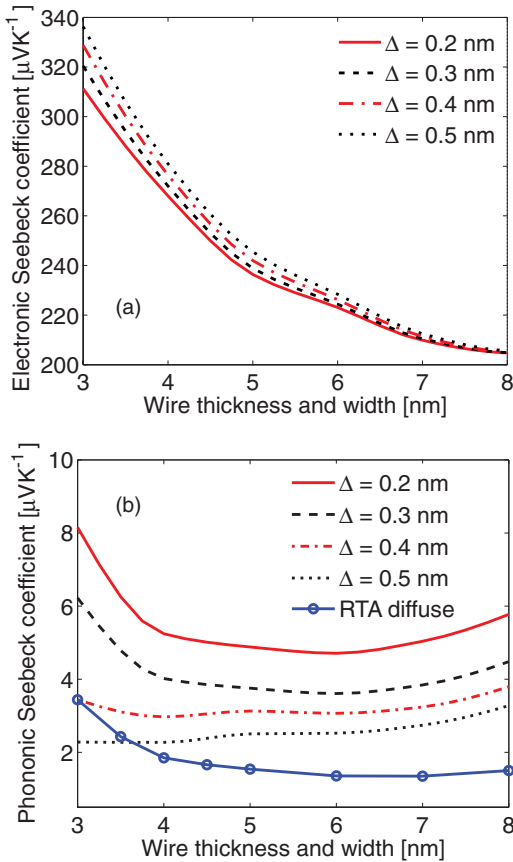


FIG. 6. (Color online) (a) Electronic and (b) phononic (i.e., phonon-drag) components of the Seebeck coefficient as a function of the SiNW cross section and rms roughness Δ . The electronic component of the Seebeck coefficient is more than an order of magnitude greater than the phonon-drag component. The phonon-drag component of S decreases with increasing roughness at the interface because of the decrease in the mean-free path of phonons.

With decreasing wire cross section, γ and τ_{ph} decrease monotonically because of the increasing relative importance of surface-roughness scattering with respect to internal scattering for both electron and phonon transport. The interplay of these two variations with the mobility variation (proportional to σ) determines the S_{ph} variation shown in Fig. 6(b).

The phonon-drag component decreases with increasing randomization of phonons. Therefore, the phonon-drag component decreases with increasing roughness of the surface. In fact, for $\kappa_l \sim 1 \text{ Wm}^{-1} \text{ K}^{-1}$, S_{ph} is almost two orders of magnitude smaller than that in bulk silicon and therefore becomes negligibly small. It should be noted that the above arguments and results imply that S_{ph} can not increase when κ_l decreases (in contradiction with Boukai *et al.*¹⁴).

C. Another look at confinement and the Seebeck coefficient

According to the work of Hicks and Dresselhaus,¹² a drastic enhancement of the thermoelectric figure of merit is supposed to be observed with thickness reduction in nanowires. The underlying assumptions in their work included thickness-independent mobility and thermal conductivity and a single-

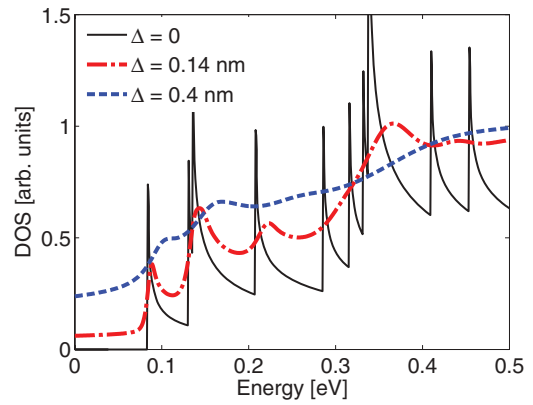


FIG. 7. (Color online) Density of states (DOS) of a $5 \times 5 \text{ nm}^2$ SiNW (black solid curve) and the effective DOS in the presence of appreciable surface-roughness scattering, for $\Delta = 0.14$ nm (red dashed-dotted curve) and $\Delta = 0.4$ nm (blue dashed curve). Roughness smears the high peaks in the DOS, thereby negating potential benefits that quantum confinement could have on the Seebeck coefficient (Ref. 71).

subband model for electrons, so the increase is connected to the sharp 1D density of electronic states peak near the subband bottom. In a system with scattering, the density of states effectively gets broadened as the levels acquire a finite lifetime.⁶⁹ The spectral density (a concept that is essentially a generalized density of states for interacting systems) can in principle be obtained from a nonequilibrium Green's function calculation with scattering accounted for.^{69,70} Here, we computed the scattering rates based on the unbroadened density of states, as is common in ensemble Monte Carlo calculations, because a fully self-consistent calculation of the scattering rates and the spectral function is computationally prohibitive.

However, we can still illustrate the influence of increasing roughness on the effective density of states in the SiNWs. In Fig. 7, we depict what surface-roughness scattering does to the density of states, where each energy level is assumed broadened according to the calculated scattering rate.⁴² Due to surface-roughness scattering, the sharp density-of-states peaks get smoothed, which would bring down the Seebeck coefficient [Fig. 6(a)] and eliminate much of the appeal that nanowires brought to the field of thermoelectrics. The smearing of DOS in ultrasmall nanostructures due to roughness has been experimentally demonstrated using x-ray absorption spectroscopy.⁷¹

V. FIGURE OF MERIT ZT

Once electrical conductivity σ , the Seebeck coefficient S , and thermal conductivity κ have been calculated, the TE figure of merit at room temperature is calculated from $ZT = S^2\sigma/\kappa T$. Figure 8 shows the variation of ZT with the wire cross section. The ZT in SiNWs is larger than that in bulk silicon; the enhancement comes primarily because of nearly two orders of magnitude decrease in the lattice thermal conductivity owing to strong phonon-boundary scattering and not to an enhancement in the power factor. ZT does not increase dramatically with decreasing wire cross section

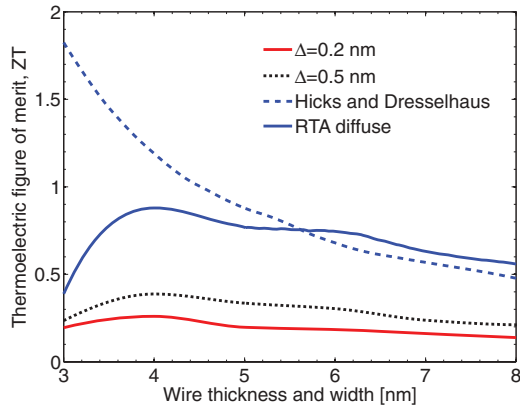


FIG. 8. (Color online) Variation of ZT with the SiNW cross section. ZT incorporating thermal conductivity from phonon Monte Carlo with real-space roughness is presented for rms roughness $\Delta = 0.2$ nm (red solid curve) and $\Delta = 0.5$ nm (dotted black curve). ZT obtained from the RTA assuming completely diffuse boundary scattering for phonons (specularity parameter equal to zero; solid blue curve) overestimates ZT .

as predicted by Hicks and Dresselhaus,¹² where a single subband and mobility independent of cross section were assumed; rather, roughening (apart from degrading thermal conductivity) severely degrades electrical conductivity, so the power factor drops with decreasing thickness. Overall, ZT has a broad peak of about 0.5 at the thickness of 4 nm for the reasonable rms roughness of 0.5 nm.

It is also interesting to note the curve that corresponds to the approximation of fully diffuse boundary scattering of phonons, where the rough interface is replaced by a specularity parameter equal to zero [Eq. (11)]. This curve gives a ZT close to 1, but would correspond to rms roughnesses of about 3 nm,¹⁶ which is unrealistic in ultrathin wires without damaging them.

Finally, let us reiterate that this paper focuses on elucidating the interplay between confinement and roughness in ultrathin nanowires for thermoelectric applications. For this purpose, all the data in this paper were presented for a single doping density $1.6 \times 10^{19} \text{ cm}^{-3}$, following Boukai *et al.*,¹⁴ as the doping densities of this order of magnitude are known to maximize the figure of merit in bulk silicon. However, in nanostructures, there is a dependence of the thermoelectric parameters on the doping density, as discussed, for instance, recently and in detail by Neophytou and Kosina.³⁴

So, for completeness, in Fig. 9 we show the dependence of the thermoelectric figure of merit of silicon nanowires with different cross-sectional features and the maximal rms roughness ($\Delta = 0.5$ nm) as a function of the carrier density. The range of carrier densities captures peak ZT values for all the wires considered in this study. While it might be tempting to strive to hit the peak value of ZT by picking the appropriate doping density, one should not forget that controlling the doping density becomes exceedingly difficult in nanostructures in which there are very few dopants: the number of dopants N has a statistical uncertainty of \sqrt{N} . For instance, in a wire of 5 nm thickness/width and 100 nm length, doped to 10^{19} cm^{-3} , there are only $N = 25$ dopants,

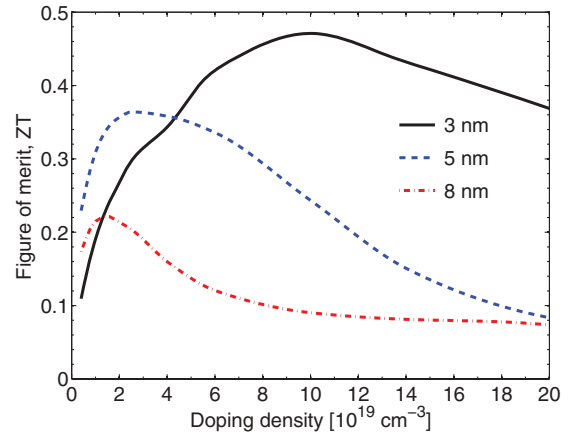


FIG. 9. (Color online) Variation of ZT with the doping density for different SiNW thicknesses. $\Delta = 0.5$ nm.

with $\sqrt{N} = 5$, so we really can not control the doping density better than about 20%.

VI. CONCLUSION

Realistic ensemble Monte Carlo simulations of electron and phonon transport in ultrathin silicon nanowires were performed to calculate the thermoelectric coefficients and the figure of merit ZT in SiNWs. The electrical conductivity decreases with decreasing wire cross section because of the strong increase in electron scattering with surface roughness and phonons. For a given carrier density and with increasing confinement, the energy separation between the conduction band edge and the Fermi level increases, resulting in an increase in the average energy carried by electrons; therefore, the electronic Seebeck coefficient increases as the wire cross section decreases. The phonon-drag component of the Seebeck coefficient is negligibly small in SiNWs because of a very short phonon mean-free path. Overall, the power factor does not show orders-of-magnitude increase with decreasing wire cross section, as predicted by earlier theoretical studies, because the decrease in electrical conductivity with decreasing thickness offsets the increase in the Seebeck coefficient. Also, as in bulk silicon, the electronic contribution to thermal conductivity is more than an order of magnitude smaller than the contribution from phonons.

The ZT in SiNWs calculated from this thermoelectric simulation is 20–40 times larger than that in bulk silicon: the enhancement in ZT occurs primarily because of the decrease in the lattice thermal conductivity due to strong phonon-boundary scattering and not due to an enhancement in the power factor. It is extremely important to account for the actual rough surface when solving the electron and phonon BTE in order to properly estimate ZT in nanostructures. For easy reference, a summary of calculated data is presented in Table I.

Greater relative advances in the power factor ought to be expected in ultrathin p -type SiNWs than in n -type ones because for hole transport conductivity does not drop as dramatically with increasing confinement as it does for electrons. The reason is that phonon-mediated intersubband scattering for holes plays a dominant role over SRS down to

TABLE I. Summary table: electrical conductivity σ , lattice thermal conductivity κ_l , electronic thermal conductivity κ_e , the electronic Seebeck coefficient S_e , the phonon-drag Seebeck coefficient S_{ph} , and the figure of merit ZT for n -type Si nanowires doped to $1.6 \times 10^{19} \text{ cm}^{-3}$, given as a function of the nanowire thickness ranging from 3 to 8 nm and for values of the surface rms roughness Δ (given in the rightmost column) ranging from 0.2 to 0.5 nm.

	Nanowire thickness (nm)						Δ (nm)↓
	3	4	5	6	7	8	
σ (10^4 S/m)	2.0	5.1	6.6	8.4	9.1	9.5	0.2
	1.6	4.4	6.0	8.0	8.7	9.1	0.3
	1.3	3.8	5.3	7.3	8.1	8.6	0.4
	0.9	3.2	4.7	6.7	7.6	8.0	0.5
κ_l (W/m K)	3.0	4.2	5.6	6.7	7.4	8.7	0.2
	2.3	3.1	3.9	5.1	5.6	6.7	0.3
	1.6	2.4	3.1	3.9	4.7	5.7	0.4
	1.2	1.9	2.4	3.3	4.1	4.6	0.5
κ_e (W/m K)	0.07	0.14	0.23	0.31	0.38	0.45	0.2
	0.06	0.13	0.21	0.29	0.36	0.43	0.3
	0.05	0.11	0.19	0.27	0.33	0.40	0.4
	0.04	0.10	0.17	0.25	0.31	0.38	0.5
S_e ($\mu\text{V/K}$)	310	270	240	220	210	200	0.2
	320	270	240	220	210	200	0.3
	330	280	240	230	210	200	0.4
	340	280	240	230	210	200	0.5
S_{ph} ($\mu\text{V/K}$)	8.2	5.2	4.9	4.7	5.0	5.8	0.2
	6.2	4.0	3.8	3.6	3.8	4.5	0.3
	3.4	3.0	3.1	3.1	3.3	3.8	0.4
	2.3	2.3	2.5	2.5	2.8	3.3	0.5
ZT	0.20	0.26	0.20	0.18	0.16	0.14	0.2
	0.22	0.31	0.26	0.23	0.20	0.17	0.3
	0.26	0.36	0.29	0.27	0.22	0.18	0.4
	0.24	0.39	0.34	0.30	0.24	0.22	0.5

very small thicknesses, as demonstrated experimentally⁷² and also known theoretically from work on ultrathin SOI.⁷³ Finally, further improvements in the power factor of both n - and p -type SiNWs could be achieved by elimination of impurity scattering, such as through modulation doping, gating,⁷² or surface transfer doping⁷⁴ as a means of achieving desired carrier densities.

ACKNOWLEDGMENTS

The authors thank N. Nishiguchi, A. Mittal, S. Mazumder, J.-J. Wu, and Z. Aksamija for helpful discussions. This work has been supported in part by AFOSR (YIP Program, award No. FA9550-09-1-0230) and by the National Science Foundation, through award No. ECCS-1201311 and the University of Wisconsin MRSEC (NSF awards DMR-0520527 and DMR-1121288).

APPENDIX: IMPURITY SCATTERING

Coulomb potential due to an ionized impurity of charge Ze , located at $\mathbf{R}(y_0, z_0)$ from the center of the wire cross section,

felt by an electron at position $[\mathbf{r}(y, z), x]$ is given by

$$U(\mathbf{r}, x) = -\frac{Ze^2}{4\pi\epsilon_{si}\sqrt{(\mathbf{r}-\mathbf{R})^2+x^2}}e^{-\frac{\sqrt{(\mathbf{r}-\mathbf{R})^2+x^2}}{L_d}}, \quad (\text{A1})$$

where ϵ_{si} is the dielectric constant of silicon and L_d is the degenerate Thomas-Fermi screening length.^{55,56} The matrix element for the impurity-electron scattering can be written as

$$\begin{aligned} M_{nm}(\mathbf{k}_x, \mathbf{k}'_x) = & -\frac{Ze^2}{4\pi\epsilon_{si}} \iint \psi_n(y, z) \\ & \times \left[\frac{1}{L_x} \int \frac{e^{i(k_x - k'_x)x} e^{-\frac{\sqrt{(\mathbf{r}-\mathbf{R})^2+x^2}}{L_d}}}{\sqrt{(\mathbf{r}-\mathbf{R})^2+x^2}} dx \right] \\ & \times \psi_m(y, z) dy dz. \end{aligned} \quad (\text{A2})$$

Defining $q = |\mathbf{k}_x - \mathbf{k}'_x|$,

$$K_0(q, \mathbf{R}) = \int \frac{e^{iqx} e^{-\frac{\sqrt{(\mathbf{r}-\mathbf{R})^2+x^2}}{L_d}}}{\sqrt{(\mathbf{r}-\mathbf{R})^2+x^2}} dx, \quad (\text{A3})$$

$$I_{nm}(q, \mathbf{R}) = \iint \psi_n(y, z) K_0(q, \mathbf{R}) \psi_m(y, z) dy dz, \quad (\text{A4})$$

and \mathcal{E} and \mathcal{E}' as the initial and final energies of the scattered electron in the parabolic band approximation, the scattering rate from a single impurity using Fermi's golden rule is

$$\Gamma_{nm}^i(\mathbf{k}_x) = \frac{2\pi}{\hbar} \frac{Z^2 e^4}{16\pi^2 \epsilon_{si}^2 L_x^2} \sum_{k'_x} I_{nm}^2(q, \mathbf{R}) \delta(\mathcal{E} - \mathcal{E}'). \quad (\text{A5})$$

The total impurity-electron scattering rate due to a uniform doping density of N_a is obtained by integrating over the position \mathbf{R} of the dopants

$$\begin{aligned} \Gamma_{nm}^{\text{imp}}(\mathbf{k}_x) = & \frac{Z^2 e^4}{16\pi^2 \hbar \epsilon_{si}^2 L_x} \int d\mathbf{R} N_a L_x \\ & \times \int dk'_x I_{nm}^2(q, \mathbf{R}) \delta(\mathcal{E} - \mathcal{E}'). \end{aligned} \quad (\text{A6})$$

Adding a nonparabolicity factor α and converting the dk'_x integration to $d\mathcal{E}'$ integration, Eq. (A6) becomes

$$\Gamma_{nm}^{\text{imp}}(\mathbf{k}_x) = \frac{Z^2 e^4 N_a \sqrt{m}}{16\sqrt{2}\pi^2 \hbar^2 \epsilon_{si}^2} \frac{(1 + 2\alpha\mathcal{E}_f)}{\sqrt{\mathcal{E}_f(1 + \alpha\mathcal{E}_f)}} \int d\mathbf{R} I_{nm}^2(q_x^\pm, \mathbf{R}), \quad (\text{A7})$$

where \mathcal{E}_f is the final kinetic energy defined in Ref. 38 and $q_x^\pm = k_x \pm k'_x$ is the difference between the initial and final electron wave vectors as defined in the SRS derivation.

- *Presently with Intel Corp., Hillsboro; redwinbosco@gmail.com
[†]knezevic@engr.wisc.edu
- ¹H. J. Goldsmid, *Thermoelectric Refrigeration* (Plenum, New York, 1964).
 - ²*CRC Handbook of Thermoelectrics*, edited by D. M. Rowe (CRC Press, Boca Raton, FL, 1995).
 - ³G. Nolas, J. Sharp, and J. Goldsmid, *Thermoelectrics: Basic Principles and New Materials Developments* (Springer, New York, 2001).
 - ⁴A. Majumdar, *Science* **303**, 777 (2004).
 - ⁵F. J. DiSalvo, *Science* **285**, 703 (1999).
 - ⁶G. A. Slack, *CRC Handbook of Thermoelectrics* (CRC Press, Boca Raton, FL, 1995), pp. 407–440.
 - ⁷A. Shakouri, *Proc. IEEE* **94**, 1613 (2006).
 - ⁸C. J. Vineis, A. Shakouri, A. Majumdar, and M. G. Kanatzidis, *Adv. Mater.* **22**, 3970 (2010).
 - ⁹R. Venkatasubramanian, E. Siivola, T. Colpitts, and B. O’Quinn, *Nature (London)* **413**, 597 (2001).
 - ¹⁰T. C. Harman, P. J. Taylor, M. P. Walsh, and B. E. LaForge, *Science* **297**, 2229 (2002).
 - ¹¹G. J. Snyder and E. S. Toberer, *Nat. Mater.* **7**, 105 (2008).
 - ¹²L. D. Hicks and M. S. Dresselhaus, *Phys. Rev. B* **47**, 16631 (1993).
 - ¹³L. D. Hicks and M. S. Dresselhaus, *Phys. Rev. B* **47**, 12727 (1993).
 - ¹⁴A. I. Boukai, Y. Bunimovich, J. Tahir-Kheli, J. Yu, W. A. Goddard III, and J. R. Heath, *Nature (London)* **451**, 168 (2008).
 - ¹⁵A. I. Hochbaum, R. Chen, R. Delgado, W. Liang, E. Garnett, M. Najarian, A. Majumdar, and P. Yang, *Nature (London)* **451**, 163 (2008).
 - ¹⁶P. Martin, Z. Aksamija, E. Pop, and U. Ravaioli, *Phys. Rev. Lett.* **102**, 125503 (2009).
 - ¹⁷I. Ponomareva, D. Srivastava, and M. Menon, *Nano Lett.* **7**, 1155 (2007).
 - ¹⁸N. Papanikolaou, *J. Phys.: Condens. Matter* **20**, 135201 (2008).
 - ¹⁹D. Donadio and G. Galli, *Nano Lett.* **10**, 847 (2010).
 - ²⁰D. Donadio and G. Galli, *Phys. Rev. Lett.* **102**, 195901 (2009).
 - ²¹N. Mingo and L. Yang, *Phys. Rev. B* **68**, 245406 (2003).
 - ²²J. Wang and J.-S. Wang, *Appl. Phys. Lett.* **90**, 241908 (2007).
 - ²³T. Markussen, A.-P. Jauho, and M. Brandbyge, *Phys. Rev. B* **79**, 035415 (2009).
 - ²⁴Y. Chen, D. Li, J. R. Lukes, and A. Majumdar, *J. Heat Transfer* **127**, 1129 (2005).
 - ²⁵D. Lacroix, K. Joulain, and D. Lemonnier, *Phys. Rev. B* **72**, 064305 (2005).
 - ²⁶D. Lacroix, K. Joulain, D. Terris, and D. Lemonnier, *Appl. Phys. Lett.* **89**, 103104 (2006).
 - ²⁷N. Mingo and D. A. Broido, *Phys. Rev. Lett.* **93**, 246106 (2004).
 - ²⁸N. Mingo, L. Yang, D. Li, and A. Majumdar, *Nano Lett.* **3**, 1713 (2003).
 - ²⁹T. T. M. Vo, A. Williamson, V. Lordi, and G. Galli, *Nano Lett.* **8**, 1111 (2008).
 - ³⁰C. Jeong, R. Kim, M. Luisier, S. Datta, and M. Lundstrom, *J. Appl. Phys.* **107**, 023707 (2010).
 - ³¹R. Kim, S. Datta, and M. S. Lundstrom, *J. Appl. Phys.* **105**, 034506 (2009).
 - ³²R. Kim and M. S. Lundstrom, *J. Appl. Phys.* **110**, 034511 (2011).
 - ³³N. Neophytou, M. Wagner, H. Kosina, and S. Selberherr, *J. Electron. Mater.* **39**, 1902 (2011).
 - ³⁴N. Neophytou and H. Kosina, *Phys. Rev. B* **83**, 245305 (2011).
 - ³⁵C. Jacoboni and L. Reggiani, *Rev. Mod. Phys.* **55**, 645 (1983).
 - ³⁶M. V. Fischetti and S. E. Laux, *Phys. Rev. B* **48**, 2244 (1993).
 - ³⁷E. B. Ramayya, D. Vasileska, S. M. Goodnick, and I. Knezevic, *IEEE Trans. Nanotechnol.* **6**, 113 (2007).
 - ³⁸E. B. Ramayya, D. Vasileska, S. M. Goodnick, and I. Knezevic, *J. Appl. Phys.* **104**, 063711 (2008).
 - ³⁹T. B. Boykin, G. Klimeck, and F. Oyafuso, *Phys. Rev. B* **69**, 115201 (2004).
 - ⁴⁰H. Mera, M. Persson, Y. Niquet, and M. Bescond, in *14th International Workshop on Computational Electronics (IWCE)*, 2010 (unpublished).
 - ⁴¹T. Ando, A. B. Fowler, and F. Stern, *Rev. Mod. Phys.* **54**, 437 (1982).
 - ⁴²S. Jin, M. Fischetti, and T. Tang, *IEEE Trans. Electron Devices* **54**, 2191 (2007).
 - ⁴³S. Jin, M. V. Fischetti, and T. Tang, *J. Appl. Phys.* **102**, 083715 (2007).
 - ⁴⁴R. Prasher, T. Tong, and A. Majumdar, *Nano Lett.* **8**, 99 (2008).
 - ⁴⁵J. Wang, A. Rahman, A. Ghosh, G. Klimeck, and M. Lundstrom, *IEEE Trans. Electron Devices* **52**, 1589 (2005).
 - ⁴⁶Y. Zheng, C. Rivas, R. Lake, K. Alam, T. B. Boykin, and G. Klimeck, *IEEE Trans. Electron Devices* **52**, 1097 (2005).
 - ⁴⁷A. Buin, A. Verma, A. Svizhenko, and M. Anantram, *Nano Lett.* **8**, 760 (2008).
 - ⁴⁸R. Sajjad, K. Alam, and Q. Khosru, *Semicond. Sci. Technol.* **24**, 045023 (2009).
 - ⁴⁹<http://www.caam.rice.edu/software/ARPACK/>.
 - ⁵⁰I. Knezevic, E. B. Ramayya, D. Vasileska, and S. M. Goodnick, *J. Comput. Theor. Nanos.* **6**, 1725 (2009).
 - ⁵¹E. Ramayya and I. Knezevic, *J. Comput. Electron.* **9**, 206 (2010).
 - ⁵²P. Lugli and D. Ferry, *IEEE Trans. Electron Devices* **ED-32**, 2431 (1985).
 - ⁵³S. M. Goodnick, D. K. Ferry, C. W. Wilmsen, Z. Liliental, D. Fathy, and O. L. Krivanek, *Phys. Rev. B* **32**, 8171 (1985).
 - ⁵⁴E. B. Ramayya, D. Vasileska, S. M. Goodnick, and I. Knezevic, in *Proceedings of the 8th International Conference on Nanotechnology*, 2008 (unpublished).
 - ⁵⁵H. Kosina and G. Kaiblinger-Grujina, *Solid State Electron.* **42**, 331 (1998).
 - ⁵⁶J. Watling, L. Yang, M. Borici, R. Wilkins, A. Asenov, J. Barker, and S. Roy, *Solid State Electron.* **48**, 1337 (2004).
 - ⁵⁷E. B. Ramayya, Ph.D. thesis, University of Wisconsin-Madison, 2010.
 - ⁵⁸R. Chen, A. I. Hochbaum, P. Murphy, J. Moore, P. Yang, and A. Majumdar, *Phys. Rev. Lett.* **101**, 105501 (2008).
 - ⁵⁹R. Peterson, *J. Heat Transfer* **116**, 815 (1994).
 - ⁶⁰S. Mazumder and A. Majumdar, *J. Heat Transfer* **123**, 749 (2001).
 - ⁶¹A. Mittal and S. Mazumder, *J. Heat Transfer* **132**, 052402 (2010).
 - ⁶²M. G. Holland, *Phys. Rev. B* **132**, 2461 (1963).
 - ⁶³M. Asheghi, K. Kurabayashi, R. Kasnavi, and K. Goodson, *J. Appl. Phys.* **91**, 5079 (2002).
 - ⁶⁴J.-J. Wu, *Tribol. Int.* **33**, 47 (2000); C. Buran, M. G. Pala, M. Bescond, M. Dubois, and M. Mouis, *IEEE Trans. Electron Devices* **56**, 2186 (2009).
 - ⁶⁵E. Pop, R. Dutton, and K. Goodson, *J. Appl. Phys.* **96**, 4998 (2004).
 - ⁶⁶Z. Aksamija and I. Knezevic, *Phys. Rev. B* **82**, 045319 (2010).
 - ⁶⁷T. Klitsner, J. VanCleve, H. Fischer, and R. Pohl, *J. Heat Transfer* **38**, 7576 (1988).

- ⁶⁸X. Lü, J. H. Chu, and W. Z. Shen, *J. Appl. Phys.* **93**, 1219 (2003).
- ⁶⁹L. P. Kadanoff and G. Baym, *Quantum Statistical Mechanics* (W. A. Benjamin, New York, 1962).
- ⁷⁰H. Haug and A.-P. Jauho, *Quantum Kinetics in Transport and Optics of Semiconductors* (Springer, Berlin, 2008).
- ⁷¹F. Chen, E. Ramayya, C. Euaruksakul, F. Himpel, G. Celler, B. Ding, I. Knezevic, and M. Lagally, *ACS Nano.* **4**, 2466 (2010).
- ⁷²H. J. Ryu, Z. Aksamija, D. M. Paskiewicz, S. A. Scott, M. G. Lagally, I. Knezevic, and M. A. Eriksson, *Phys. Rev. Lett.* **105**, 256601 (2010).
- ⁷³L. Donetti, F. Gamiz, N. Rodriguez, and A. Godoy, *IEEE Electron Device Lett.* **30**, 1338 (2009).
- ⁷⁴P. Zhang, E. Tevaarwerk, B.-N. Park, D. Savage, G. Celler, I. Knezevic, P. Evans, M. Eriksson, and M. Lagally, *Nature (London)* **439**, 703 (2006).